ABSTRACT

Title of thesis: META-STRUCTURE ENHANCEMENT OF RESONANT ACOUSTIC MIXING VIA EMBEDDED ADDITIVE MANUFACTURING

William Alexander Reach, Masters of Science, 2019

Thesis directed by: Professor Ryan D. Sochol
Department of Mechanical Engineering

The performance of energetic materials is founded on a wide range of material and mixing parameters. Resonant acoustic mixing (RAM) is advantageous as a scalable, contactless energetics mixing method; however, challenges remain in connecting process parameters to post-mix performance. In this thesis, we analyzed the influence of the structural arrangement of pre-mixture ingredients (*i.e.*, the pre-mix "meta-structure") on post-mix properties. We utilized an embedded additive manufacturing strategy for ingredient loading to realize two distinct pre-mix meta-structures: (*i*) a consolidated (control) configuration, and (*ii*) a novel distributed arrangement. Following identical RAM processing, post-mix products were sectioned and optically characterized using scanning electron microscopy and electron-dispersive electron dispersive spectroscopy, revealing significant reductions in void content corresponding to the distributed meta-structure designs. Mechanical testing of post-mix products revealed distributed meta-structure specimens elongated up to 147%

more than consolidated specimens prior to fracture, suggesting a critical role for pre-mix ingredient architecture in post-RAM performance.

# META-STRUCTURE ENHANCEMENT OF RESONANT ACOUSTIC MIXING VIA EMBEDDED ADDITIVE MANUFACTURING

by

William Alexander Reach

Thesis submitted to the Faculty of the Graduate School of the
University of Maryland, College Park in partial fulfillment
of the requirements for the degree of
Masters of Science
2019

Advisor Committee:
Professor Ryan Sochol, Chair
Professor Peter Chung
Professor Siddhartha Das

# DEDICATION

To my wife Kimberly
and my children Dylan, Cole, Owen, Liam and Josephine.
Thank you for all of your support and love.

# AKNOWLEDGEMENTS

Thank you to Professor Ryan Sochol for affording me the opportunity to conduct research within your lab and working with me from halfway around the world prior to my arrival. Thank you to Michael Restaino for all of your assistance with design, execution, testing and guidance through this process. I would also like to thank all of the other personnel that worked on this project: Stoney Fentomiller, Joshua Nail and Max Sidebotham for work with G-Code, Saul Schaffer and Hannah Lobell for work with building the 3D printer, printing product and RAM processing, Isaac Dunbar printer calibration and mechanical testing. I would like to thank the Mechanical Engineering Department at the US Naval Academy for funding my M.S. in Mechanical Engineering at the University of Maryland. Lastly, thank you to the Office of Naval Research Naval Surface Warfare Center Sponsor Number N0017417C0010 for sponsoring this research.

# TABLE OF CONTENTS

# LIST OF TABLES

# LIST OF FIGURES

# LIST OF ABBREVIATIONS

| | |
|---|---|
| AVA | Average Void Area |
| $DC_i$ | Darkness Content of a single imaged sample |
| $DC_{min}$ | Minimum observed Darkness Content for all of the imaged samples |
| $DC_{max}$ | Maximum observed Darkness Content for all of the imaged samples |
| EDS | Electron-Dispersive X-ray Spectroscopy |
| HTPB | Hydroxy-Terminated-Polybutadiene |
| IDP | Isodecyl Pelargonate |
| IDPI | Isophorone Diisocyanate |
| L/D | Length/Diameter |
| PBX | Polymer-Bonded Explosive |
| PSP | Process Structure Performance |
| SEM | Scanning Electron Microscopy |
| RAM | Resonant Acoustic Mixing |
| RVC | Relative Void Content |
| VA | Void Area |

# 1. INTRODUCTION

Of late, RAM has emerged as a worthwhile approach to overcome the limitations of traditional methods that rely on hand mixing and/or impeller blades [1-3]. For example, it is possible that the specific manner in which energetic formulation ingredients are loaded into the mix vessel could unintentionally disrupt the mixing efficacy, thereby negatively effecting post-mix performance. A promising extension of this possibility, however, is that by elucidating the process-structure-performance (PSP) relationships underlying RAM, pre-mix meta-structures could be designed to work synergistically with RAM to ultimately improve binder-filler interactions, reduce material defects, increase batch-to-batch repeatability, tune initiation sensitivity, and/or enhance additional metrics of energetic performance.

The use of RAM for energetics processing offers promising means to improve energetic material homogeneity, and, in turn, performance; however, the vast majority of experimental investigations of RAM in academia have stemmed more from pharmaceutical applications [4-8] than energetics processing [1, 9]. Nonetheless, several conclusions of studies in both areas have been consistent. First, RAM leads to better mixing performance compared to conventional mixing approaches [1-3]. Second, RAM provides a uniquely scalable technology for which experimental conditions in the lab are directly applicable to large-scale RAM capabilities [9, 10]. Third, highly repeatable protocols for pre-mix ingredient loading and RAM processing—with minimal undesired variations associated with these steps—are critical to experimental investigations of RAM [11–14]. Research and engineering

challenges stem particularly from unintended disparities in the initial deposition of pre-mix ingredients into the mix vessel (*i.e.*, directly prior to RAM processing). The ability to produce reliable mixed products is predicated on eliminating variations in structure and performance that are brought about by variations in the handling of pre-mix ingredients. At present, mix ingredients are typically loaded in a bulk manner, which entails manually weighing distinct mix ingredients, and then depositing groupings of ingredients into the mix vessel through set routines [1, 9]. To produce consistent pre-mix results, we utilized an embedded additive manufacturing technique in which the solid particles are placed in the container first and then discrete aliquots are placed in specific locations via a multi-material 3D printer. Embedded additive manufacturing (*i.e.* embedded 3D printing) is a fast-growing method that allows the precision of 3D printing to be used for precise placement of multiple liquid agents in a container of solid particles [15-19]

In this project, we experimentally investigated the potential connections between the relative arrangement of pre-mix formulation ingredients and post-RAM processing outcomes through a three-pronged approach: (*i*) developing a novel embedded additive manufacturing (or *embedded three-dimensional (3D) printing*) strategy for loading formulation ingredients of polymer-bonded explosive (PBX) simulants in vessels with distributed pre-mix meta-structures; (*ii*) optically characterizing the post-RAM material composition *via* scanning electron microscopy (SEM) and electron-dispersive X-ray spectroscopy (EDS) analysis; and (*iii*) mechanically evaluating the post-mix performance through axial tensile testing.

# 2. MATERIALS AND METHODS

## 2.1. CONVENTIONAL METHOD

The standard, or conventional, protocol used for pre-mix ingredient loading entails (**Figure 1**): (*i*) first depositing ~40-60% of the solid surrogate simulant particles; (*ii*) loading the bulk liquids, including polymers, plasticizers, and wetting agents; (*iii*) depositing the remaining solid surrogate simulant particles; and then (*iv*) loading the curing agent. It is important to note that the relative positioning of the curing agent and bulk liquids is motivated by the condition that these sets of ingredients remain independent from one another until RAM initiation, to prevent premature curing of the polymer prior to solids wetting. This relative spatial arrangement of the solids, bulk liquids, and curing agent (**Figure 1**– *right*) can be classified as the pre-mix meta-structure.

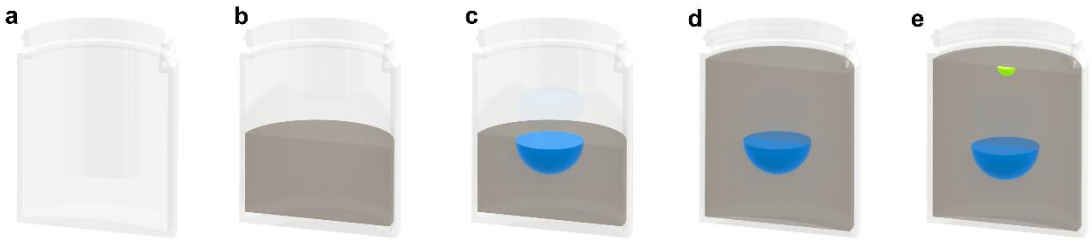


**Figure 1:** Conceptual illustrations of the standard protocol used for the loading of discrete groupings of energetic surrogate formulation ingredients, including (*blue*) polymer, plasticizer, and wetting agent, and (*green*) curing agent, into a mix vessel in preparation for subsequent resonant acoustic mixing (RAM). **(a)** Empty jar, **(b)** jar with half of the surrogate solid particles loaded, **(c)** bulk aliquot manually added, **(d)** remaining surrogate solid particles added, **(e)** curative aliquot manually added.

## 2.2. PBX SIMULANT MATERIAL PREPARATION

The bulk liquid components consisted of 14.8g hydroxy-terminated polybutadiene (HTPB) resin (Sigma-Aldrich, St. Louis, MO), 14.7g isodecyl pelargonate (IDP) plasticizer (Rocket Motor Components, Cedar City, UT), and 2.56g vegetable derived lecithin (Fisher Scientific, Fair Lawn, NJ) wetting agent, and was used in a 11.1:1 ratio to the curing agent, isophorone diisocyanate (IDPI) (Sigma-Aldrich, St. Louis, MO), which made up 1.33g of the total meta-structure mass. The bulk liquid mix was created by first combining lecithin and IDP then vortexing for two minutes followed by sonication for one hour. HTPB was heated to 65°C and subsequently added to the lecithin-IDP mixture and sonicated overnight. The explosive particle simulate was comprised of 200g of granulated cane sugar (Domino Foods Inc, Yonkers, NY) that was processed to reduce its grain size. The reduced sugar was then sifted through a 300 μm sieve (Advantech No. 50, Fisher Scientific, Hampton, NH) and a maximum post-sieve grain size of 300 μm was verified with optical imaging.

## 2.3. EMBEDDED ADDITIVE MANUFACTURING STRATEGY

In order to obtain batch-to-batch repeatability for the pre-mix meta-structure, we built a custom, dual-nozzle, multi-material 3D printer (MakerFarm) (**Figure 2a)** capable of discretely depositing bulk liquid aliquots comprising of HTPB-IDP-lecithin wetting agent, as well as curing agent aliquots of IPDI within a matrix of inert solid microparticles (*i.e.*, size-filtered sugar). Then, we loaded the HTPB-IDP-lecithin in one syringe (**Figure 2b-**right**)**, the bulk agent, and the IPDI curing agent in a separate syringe (**Figure 2b-**left**)**.

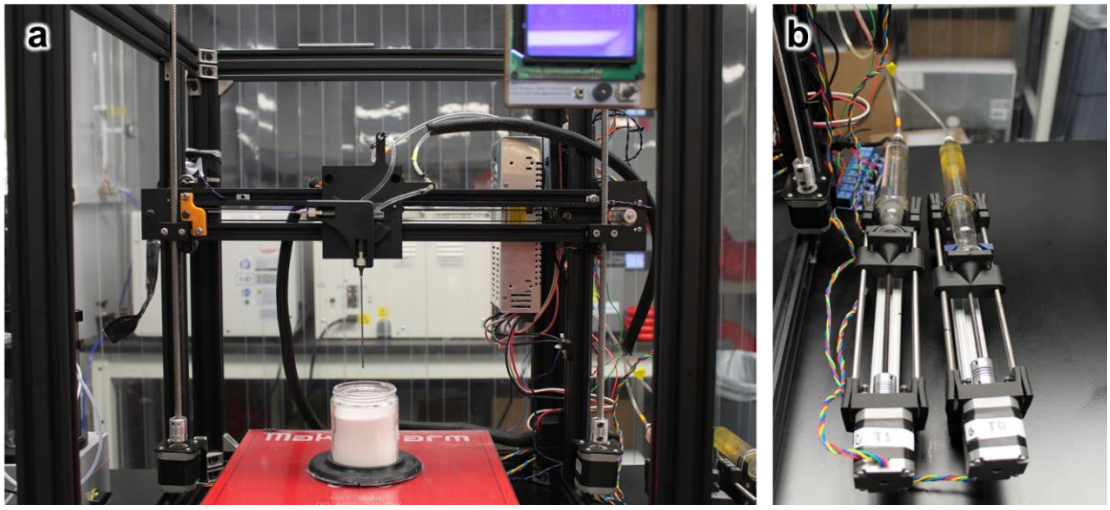


**Figure 2:** Modified open source 3D printer set-up utilized for embedded additive manufacturing of both the consolidated and distributed pre-mix meta-structures. **(a)** 3D printer with dual nozzle rotating print head capable of X, Y and Z axis control. **(b)** syringes utilized for controlling the extrusion of bulk (right) and curative (left).

This pre-mix embedded additive manufacturing approach entails first loading all of the solid surrogate microparticles, and then utilizing a dual-nozzle rotational assembly to deliver bulk liquid aliquots comprising of HTPB-IDP-lecithin wetting agent using one nozzle, and IPDI curing agent aliquots through a different nozzle, for embedded deposition inside a matrix of solid inert microparticles (**Figure 2**). It is important to note that both meta-structures included identical total volumes of solids, polymers, plasticizers, wetting agents, and curing agents. However, the consolidated meta-structure deposits these volumes in a single aliquot for each bulk and curative, 35.3ml and 1.3ml respectively, (**Figure 3**), whereas, the distributed meta-structure included these volumes dispersed among the numerous smaller aliquots, 2.52ml bulk and 0.1ml curative, within the solids surrogate matrix (**Figure 4**).

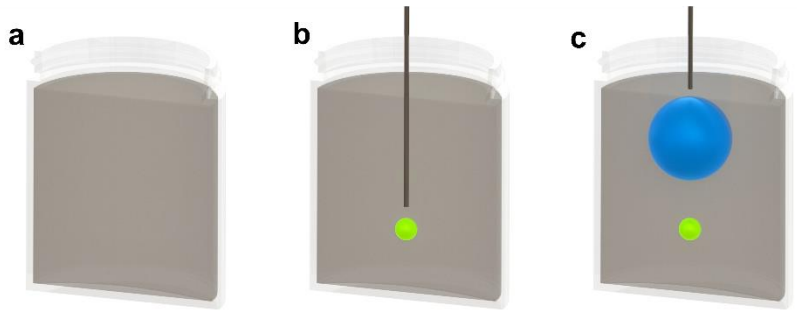


**Figure 3:** Conceptual illustrations of a consolidated protocol for the embedded loading of discrete groupings of energetic surrogate formulation ingredients, including (*blue*) polymer, plasticizer, and wetting agent, and (*green*) curing agent, into a mix vessel in preparation for subsequent resonant acoustic mixing (RAM). **(a)** jar filled with surrogate solid particles, **(b)** extruded curative aliquot, **(c)** extruded bulk aliquot.

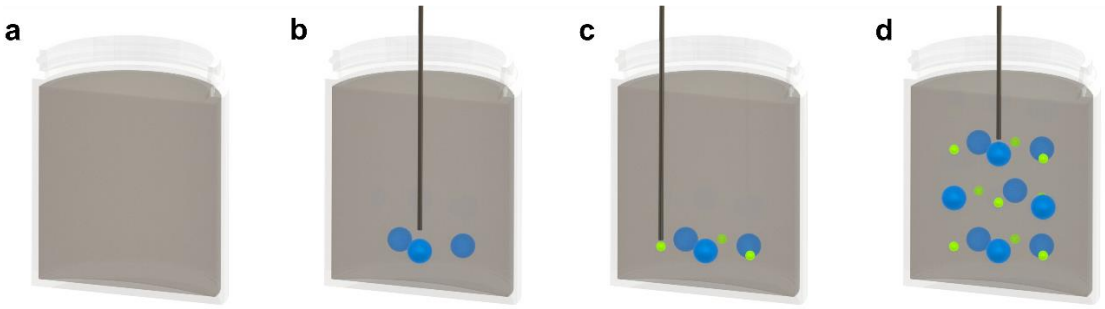


**Figure 4:** Conceptual illustrations of a distributed meta-structure multi-nozzle embedded additive manufacturing protocol for the loading of energetic formulation ingredients into the mix vessel in preparation for RAM processing. This embedded additive manufacturing strategy allows for distinct aliquots of the (*blue*) bulk liquid (*e.g.*, polymer, plasticizer, and wetting agent) and (*green*) curing agent to be precisely positioned with aliquot-specific control of volume to achieve distributed pre-mix meta-structures. **(a)** jar with surrogate solids loaded, **(b)** extruding first bulk layer, **(c)** extruding first curative layer, **(d)** extruding final aliquot.

Experimental results for loading of the bulk liquid and curing agent aliquots revealed an extruded volume accuracy of ±1.09% and ±2.25%, respectively. Using G-code, the custom-built 3D printer (**Figure 5a** – right), and the loaded materials, we utilized embedded 3D printing for each pre-mix meta-structure as desired.

## 2.4. RAM PROCESSING

Following completion of the meta-structure embedded 3D printing process, we transferred the pre-mix to a LabRAM (**Figure 5a**–left) and secured the samples with the integrated vacuum chamber (**Figure 5b, c**). Once secure, we initiated a mixing protocol (**Figure 5d**)—suggested by the LabRAM manufacturer (Resodyn Acoustic Mixers)—that was identical for both pre-mix meta-structures. The RAM protocol consisted of the following: (1) 30 seconds at 30 G's, (2) 1 minute at 80 G's, (3) establish vacuum while at 10 G's for 90 seconds, (4) 30 seconds at 30 G's, (5) 30 seconds at 50 G's and 30 seconds at 80 G's. As shown in **Figure 6c**, following RAM processing, the pre-mix meta-structure will, theoretically, consist of a homogeneous mixture.

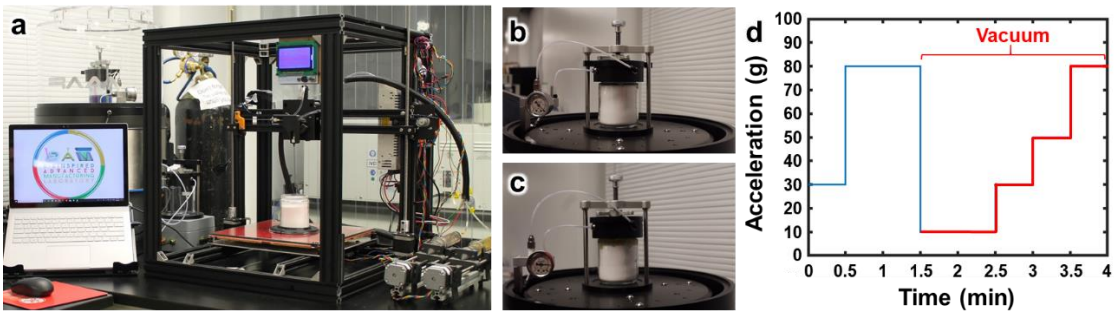


**Figure 5:** RAM processing protocol. **(a)** LabRAM and 3D Printer bench-top set-up. **(b, c)** Both the distributed **(b)** and consolidated **(c)** pre-mix meta-structures loaded into the LabRAM with integrated vacuum chamber prior to mixing initiation. **(d)** RAM parameters utilized for both pre-mix meta-structures.

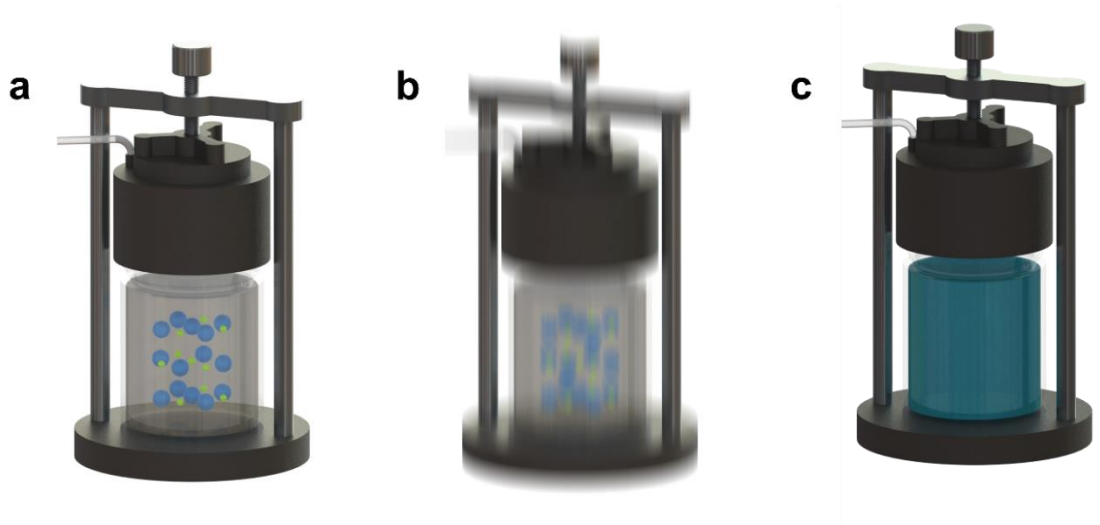


**Figure 6:** Conceptual illustration of RAM processing for distributed meta-structure: **(a)** completed print of distributed pre-mix meta-structure is secured in RAM, **(b)** distributed meta-structure experiences up to 80 G's of acceleration during mixing process, **(c)** following RAM processing the meta-structure is uniformly mixed yielding, theoretically, a homogeneous structure.

## 2.5. Optical and Mechanical Characterization

After RAM processing, we evaluated post-mix outcomes both optically and mechanically. For mechanical characterization, we loaded the post-mix into 3D printed dog bone molds (**Figure 7**), which were placed inside a fabricated container on a hot plate set to cure at 65 ℃ for one week to support full thermal curing. We monitored the temperature of the dog bones using an infrared thermometer throughout the curing phase to ensure the temperature remained at 65±5 ℃. Once the dog bone specimens corresponding to both meta-structures fully cured, we utilized an Instron 3345 testing system equipped with a pneumatic side action grip for thin polymer films to apply axial loads at a rate of 5 mm/min at 20 °C to the specimens until fracture.

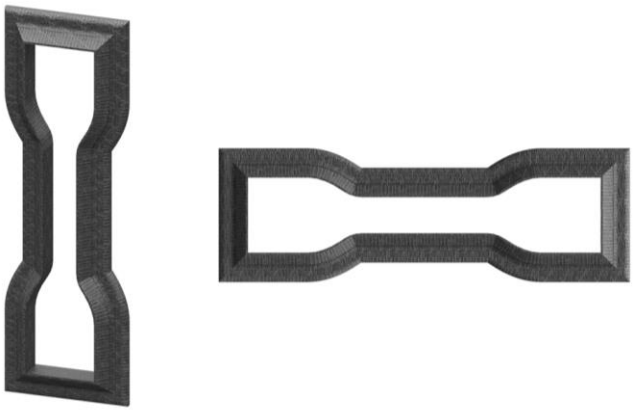

**Figure 7:** 3D printed dog bones utilized as molds to form the test specimen from the post-mix material for consolidated and distributed pre-mix meta-structures to allow for mechanical characterization.

For optical characterization, we obtained core samples from the center of the post-mix product, which were sectioned corresponding to their relative location along the height of the mix (*i.e.*, bottom, middle, and top). This process resulted in two specimens per tier for the bottom, middle, and top—six specimens total per meta-structure. We then utilized a Tescan GAIA FIB/SEM, with SEM with EDS capabilities, to optically characterize the microstructure and material composition of the sectioned specimens using 15 scans for each image achieving a penetration depth of 2-3μm.

# 3. RESULTS AND DISCUSSION

## 3.1. MANUFACTURING PROCESS

Due to the wetting of the solids being a function of a variety of loading factors (*e.g.*, the rate of fluid deposition, the time between each loading step and RAM initiation, *etc.*), the implementation of pre-mix loading *via* manual means can introduce undesired irregularities that are detrimental to mixing and limit batch-to-batch repeatability [2,3]. In addition, pre-mix meta-structures with relatively binary bulk distributions can negatively affect mixing efficacy, presenting critical barriers to particular applications that require mixing in vessels with large length/diameter (L/D) ratios or alternative complex geometries (*e.g.*, mix-in-case) [20]. Consequently, novel techniques that minimize the overall process variability are critical to enabling systematic studies of the role of pre-mix meta-structure in RAM processing and post-mix outcomes.

To facilitate embedded 3D printing of each pre-mix meta-structure, we programmed G-code (similar to **APPENDIX A: Example of G-Code** and **Figure 8**) for the 3D printer, which dictates the X, Y, and Z-Axis placement of the deposition nozzle relative to the mix vessel as well as the material deposition dynamics. The use of G-code allowed for finite control of print head location as well as, accurate control of the amount of agent being extruded in to the solid surrogate particles. The speed of the step motor used to control the deposition of liquid agents (i.e. bulk and curative agents) was reduced to prevent any liquid agents from traveling up the side of the needle during the extrusion process. A similar reduction in step motor speed was required during the retraction of the needle from the surrogate particles to prevent the

inadvertent movement of any liquid agents to ensure aliquots remained in their intended location.

```
M117 B | L | First Layer
M42 P57 S255
G4 S2
G1 X-12.056 Y-12.056
G1 Z-43 F100
G1 E134.34 F1000
G4 S15
G1 E134.34 F1000
G4 S15
G1 Z43 F4000
```

**Figure 8:** Sample of open source G-code utilized for control of the custom 3D printer X, Y, Z axis control as well as control of extrusion of syringe to deposition of bulk liquids including polymers, plasticizers, and wetting agents.

The special controls for position, speed and deposition of material for the 3D printer were obtained by coding similar to that shown in **Figure 8**. The code G1, will control the signal for step motors that position the print head, base platform or extrusion of liquid agents. Following G1 will be a letter that corresponds to which step motor to operate. For instance, X-12.056 initiates a command to the step motor for the X-plane and will operate until its final position is obtained (**Figure 8**). The next part of the code will have a F designator followed by a numerical value that will dictate the rate at which the step motor operates, or printer repositions in this case. The magnitude of the value following the F designator corresponds to the rate, the larger the value the faster the step motor will operate. As discussed earlier the rate at which we operated the print head into and out of the solid surrogate materials compared to repositioning for the next extrusion were different, as well as the rate at which we extrude liquid agents and can be seen in the example shown in **Figure 4**. The rate of F4000 is used for X and Y

positioning while the rate of F1000 is used for Z positioning, and the code F100 is used for the rate of liquid extrusion (**Figure 8**).

We then developed a novel embedded additive manufacturing strategy for energetic surrogates to enable the strategic pre-placement of formulation ingredients prior to RAM processing in an effort to improve the precision of experimental studies connecting pre-mix meta-structure to post-mix outcomes. This process can be designed to ensure that specific components of the pre-mix meta-structure (*i.e.*, the curing agent and the polymer-plasticizer) are restricted from interacting until RAM initiation to promote solids wetting. The 3D printer can be programmed to support the implementation of a wide variety of pre-mix meta-structures with respect to the specific placement of the curing agent and polymer-plasticizer volumes with respect to each other and the micro-particles. In addition, the tasks of ingredient measurement and deposition are fully automated, thereby improving process metrics associated with time, labor, and batch-to-batch repeatability.

To investigate the PSP relationships among embedded additive manufacturing-enabled pre-mix meta-structures, RAM processing, and post-mix performance, we executed a multi-step process. First, we created two highly distinct meta-structures to serve as fundamental examples for experimental testing: (*i*), a standard protocol-inspired consolidated meta-structure, which included one curing agent aliquot of IPDI in the center and one bulk liquid aliquots comprising of HTPB-IDP-lecithin wetting agent closer to the top (**Figure 3**) and (*ii*) a distributed meta-structure, which included three rows of nine alternating aliquots **(Figure 4–** *right*).** The inversion of aliquot placement between the standard protocol and the consolidated pre-mix meta-structure

was done to prevent premature interaction of the HTPB-IDP-lecithin wetting agent with the IDPI curing agent that would occur due to the large volume of bulk aliquot that would be extruded into the center of the solid surrogate particles and travel up past the outside of the nozzle to settle on top of solid surrogate particles and interact with the curing agent prior to RAM processing. By inverting the aliquot location, the much smaller IDPI curing agent aliquot is placed in the center and is able to absorb into the solid surrogate particles and the, much larger, HTPB-IDP-lecithin wetting agent aliquot is extruded near the top of the solid surrogate particles thereby, preventing premature interaction between the bulk and curing agents.

An important performance metric for the pre-mix embedded additive manufacturing process is the ability for the 3D printer to accurately dispense liquid aliquots at target volumes. In order to investigate this capability, we performed calibration experiments corresponding to both liquids (*i.e.*, bulk liquid comprising of HTPB-IDP-lecithin wetting agent and IPDI curing agent). Because our recipe required a 11.1:1 HTPB:IDPI agent ratio, we calibrated the distinct liquids at two different orders of magnitude. The experimental results for the HTPB-IDP-lecithin liquid revealed an overall accuracy of ±1.09%. There appeared to be some increased variability for programmed extruded volumes of 0.5 ml (**Figure 9a**). The calibration results for the IPDI curing agent revealed a slightly reduced accuracy of ±2.25%, although this was likely due to the significantly smaller dispensed volumes (*i.e.*, in the range of 0.01 to 0.05 ml) (**Figure 9b**).

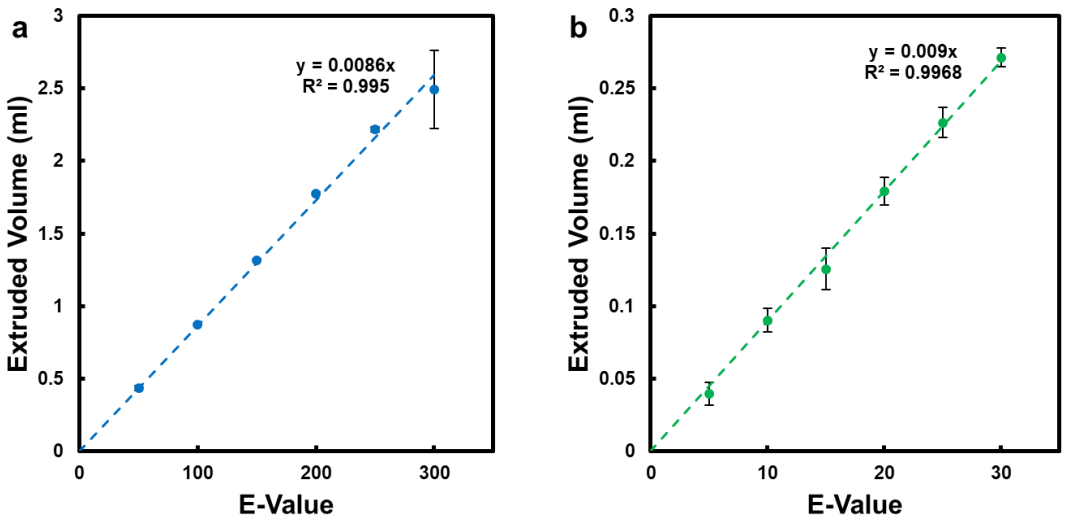


**Figure 9:** Experimental results for extruded volume calibration versus the E-value used in the G-code for printing of the: **(a)** HTPB-IDP-lecithin mixture, and **(b)** IPDI curing agent.

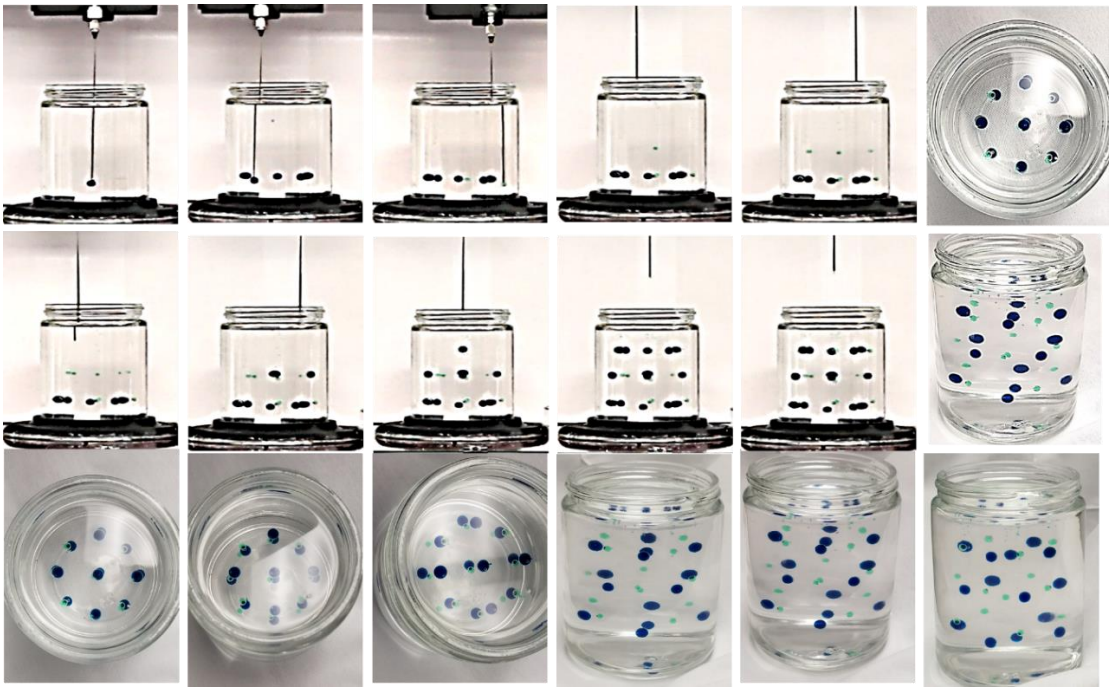

**Figure 10:** Experimental results for the dual-nozzle approach for pre-mix meta-structure embedded additive manufacturing. Proof-of-concept demonstration of the deposition process for distinct liquid aliquots representing the (*blue*) bulk liquid and (*green*) curing agent within a glycerol matrix.

To assess the dual-nozzle deposition capabilities of the 3D printer, we executed a proof-of-concept distributed pre-mix meta-structure embedded additive

manufacturing demonstration utilizing distinct dye-colored deionized water aliquots and a HTPB matrix for visualization purposes (**Figure 10**). After observing the successful multi-material fluid delivery and placement, we utilized the custom 3D printer along with the experimentally obtained calibration curves (**Figure 9**) to conduct embedded 3D printing of both the consolidated pre-mix meta-structures (**Figure 11**) and the distributed pre-mix meta-structures (**Figure 12**) with HTPB-IDP-lecithin aliquots and IPDI aliquots delivered in a matrix of solid surrogate microparticles.

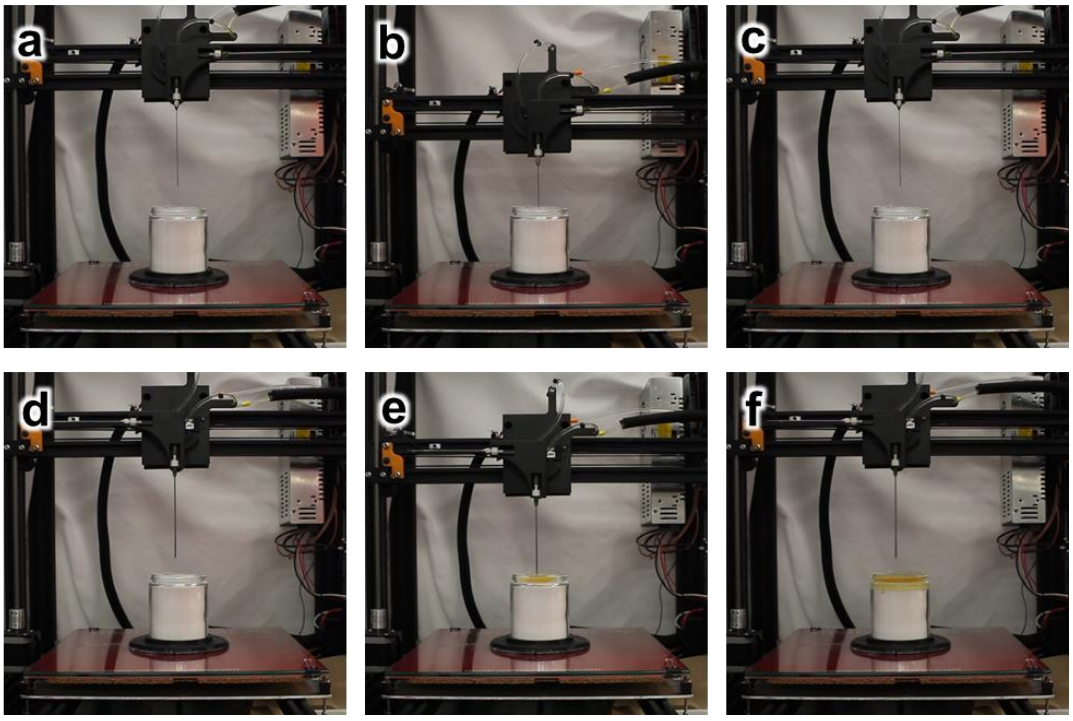


**Figure 11:** Demonstration of dual-nozzle embedded additive manufacturing of consolidated pre-mix meta-structure: **(a)** Start print, **(b)** print curative layer, **(c)** print moves up, **(d)** dual print head rotates, **(e)** print bulk layer, **(f)** print complete.

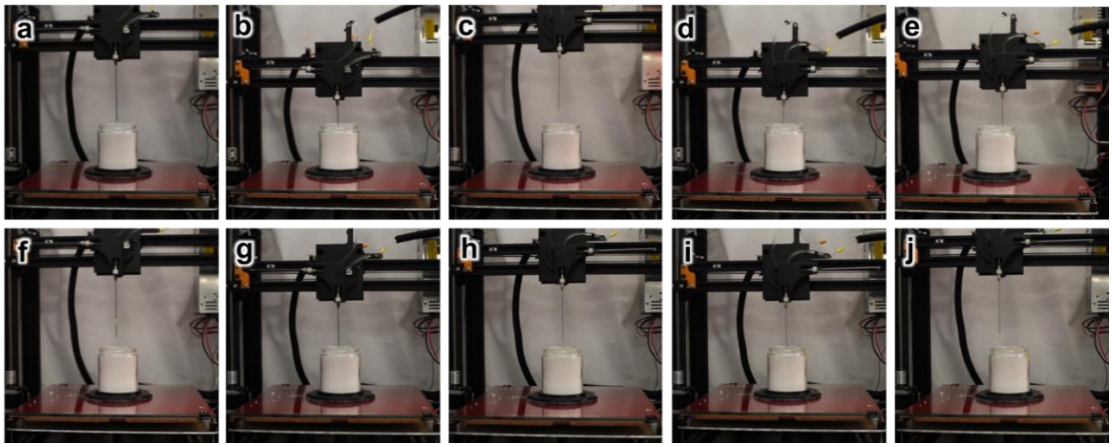


**Figure 12:** Demonstration of dual-nozzle embedded additive manufacturing of distributed pre-mix meta-structure: **(a)** Start print, **(b)** print first bulk layer, **(c)** dual print head rotates, **(d)** print first curative layer, **(e)** print second curative layer, **(f)** dual print head rotates, **(g)** print third bulk layer, **(h)** dual print head rotates, **(i)** print third curative layer, **(j)** print complete.

Once the print process was completed, the pre-mix meta-structure were transferred to a LabRAM for mixing (**Figure 13**). The procedure utilized for mixing was that which was recommend from Resodyn and is graphically shown in **Figure 13c**. The conceptual mixing from use of the LabRAM can be seen in **Figure 6** and should, theoretically, result in a near homogenous structure when complete. Each pre-mix meta-structure was mixed following the same procedure in order to minimize processing differences so that any variations in homogeneity and PSP would be due to effects from the pre-mix meta-structure following RAM processing.

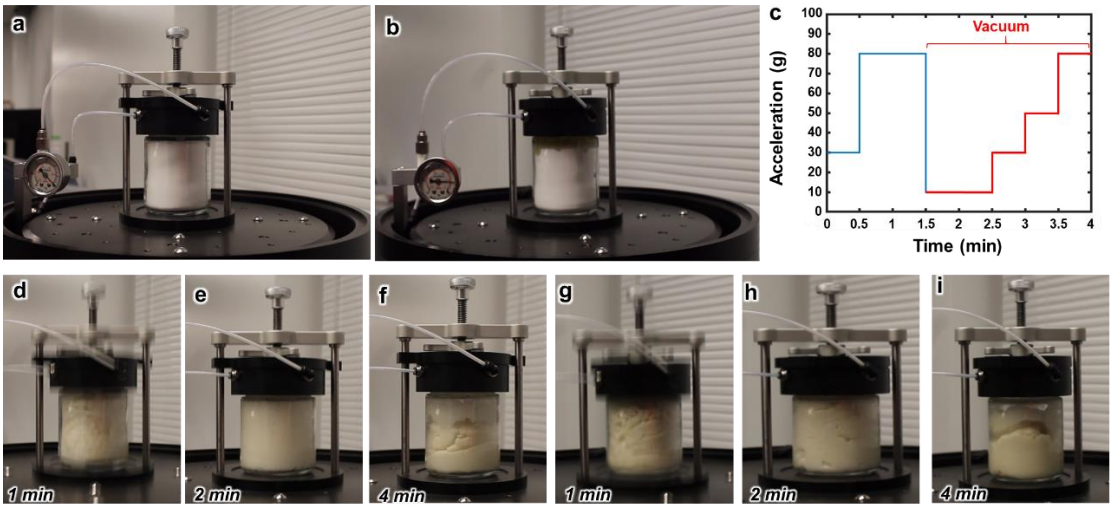


**Figure 13: (a)** Distributed meta-structure in RAM, **(b)** consolidated meta-structure in RAM, **(c)** mixing protocol implemented with LabRAM labeled with key mixing events, **(d, e, f)** distributed meta-structure when mixture becomes fully wetted, cohesive, and completed, respectively, **(g, h, i)** consolidated meta-structure when mixture becomes fully wetted, cohesive, and completed, respectively.

## 3.2. Optical Characterization

Once RAM processing was completed the core of both, the consolidated and distributed, meta-structures were removed and segmented into six samples (**Figure 14**). This resulted in two samples from the top, middle, and bottom sections of both meta-structures yielding twelve samples in total. These samples were then set-up to cure as previously desctribed.

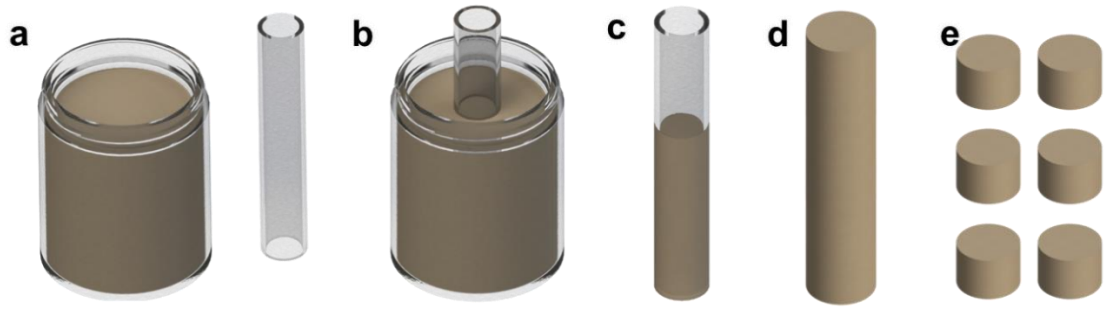


**Figure 14:** Illustration of core sampling for SEM and EDS imaging: **(a)** post RAM processing meta-structure and coring tool, **(b)** coring tool inserted into center of meta-

structure for sample, **(c)** coring tool removed from meta-structure, **(d)** sample removed from coring tool, **(e)** sample cut into six portions (2-top, 2-middle and 2-bottom).

Following RAM processing (**Figure 13**) and the coring/sectioning process (**Figure 14**), a Tescan GAIA FIB/SEM, with SEM with EDS capabilities, to optically characterize the microstructure and material composition of the sectioned specimens as previously described (**Figure 16a-f**). The area selected for EDS analysis yielded the largest square area available to allow for a more cohesive result (**Figure 15**). To evaluate the void content of the post-mix products, we utilized EDS analysis to obtain the elemental composition of the various specimens (**Figure 16g-l**).

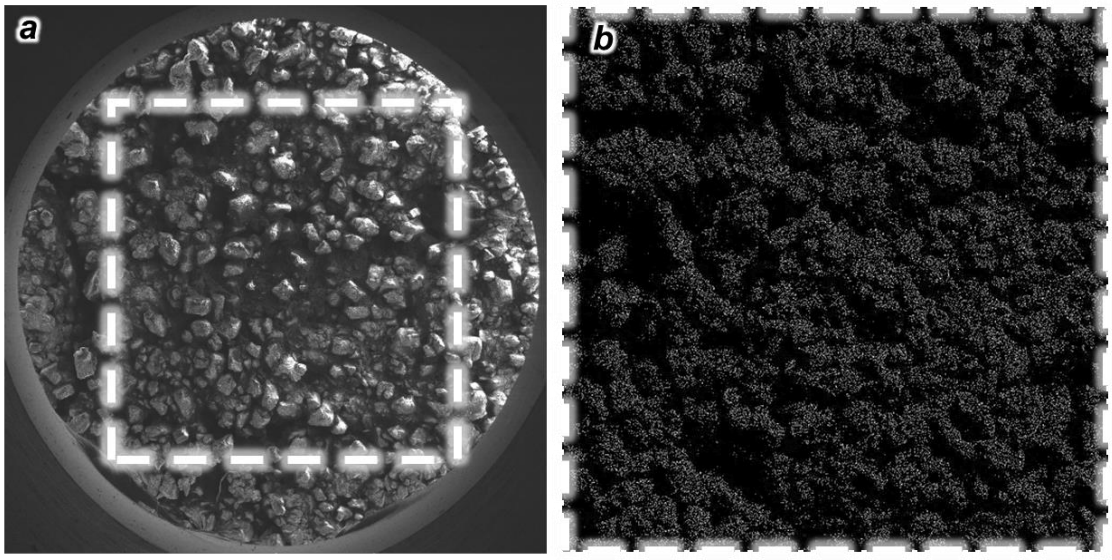


**Figure 15:** Process for selection of area to conduct EDS analysis in relation to location on SEM image. The area selected was the largest available square area to maximize area selection.

We then employed the image processing software, ImageJ (NIH), to quantify the overall lightness/darkness content corresponding to each height tier and pre-mix meta-structure design. We converted these results to a performance metric of Relative Void Content (RVC), which was calculated using previously described methods [20] as:

$$Relative\ Void\ Content\ (RVC) = \frac{DC_i - DC_{min}}{DC_{max} - DC_{min}} \qquad (1)$$

where $DC_i$ is the darkness content of a single imaged sample, $DC_{min}$ is the minimum observed darkness content for all of the imaged samples, and $DC_{max}$ is the maximum observed darkness content for all of the imaged samples. The experimental results revealed the specimens corresponding to the distributed pre-mix meta-structures consistently exhibited improved (*i.e.*, lower) RVC magnitudes compared to their consolidated counterparts (**Figure 16m**).

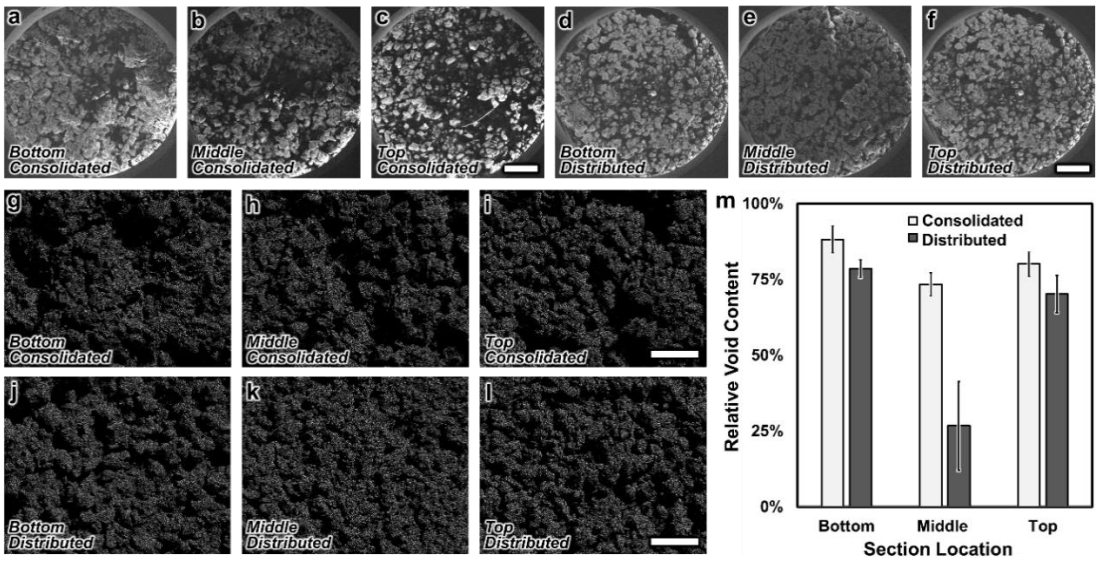


**Figure 16:** Optical characterization results for relative void content. **(a-f)** SEM of post-mix specimens at varying tiers corresponding to consolidated **(a-c)** and distributed **(d-f)** pre-mix meta-structures. Scale Bars = 1 mm. **(g-l)** EDS analysis of post-mix specimens at varying tiers corresponding to consolidated **(g-i)** and distributed **(j-l)** pre-mix meta-structures. Scale Bars = 500 $\mu$m. **(m)** Quantified results for RVC.

For example, for specimens corresponding to the bottom tier, the average RVC significantly decreased from 88.2%±4.4% for the consolidated case to 78.6%±2.9% for the distributed case ($p < 10^{-3}$). This trend was most pronounced for the middle tier, for

which the average RVC decreased from 73.4%±3.8% to 26.7±14.7% for the consolidated and distributed meta-structure cases, respectively.

To further evaluate the EDS data for void content the largest three void areas, of each sample, were measured using Photoshop and compared to each applicable height tier in order to determine any trends. The largest three void areas (VA) were then summed together and divided by the total area of the that image to calculate the Average Void Area (AVA):

$$Average\ Void\ Area\ (AVA) = \frac{\sum_{i=1}^{n} VA}{TA} \qquad (2)$$

where *TA* is the total area of the sample [21,22].

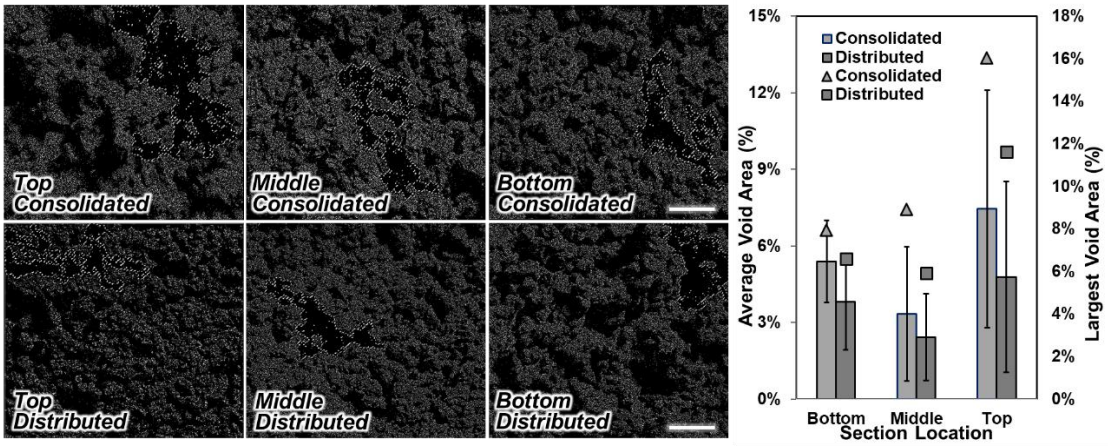


**Figure 17:** Optical characterization results for average void area. **(a-f)** EDS analysis of post-mix specimens at varying tiers corresponding to consolidated **(a-c)** and distributed **(d-f)** pre-mix meta-structures. Scale Bars = 500 $\mu$m. **(g)** Quantified results for AVA.

The experimental results followed closely to the analysis of RVC showing the specimens corresponding to the distributed pre-mix meta-structures consistently exhibited improved (*i.e.*, lower) AVA magnitudes compared to the corresponding consolidated pre-mix meta-structure samples. For specimens corresponding to the

middle tier, the AVA decreased from 3.33±2.87% for the consolidated meta-structure to 2.43±1.87% for the distributed meta-structure. The largest difference occurred in the top tier for which the AVA decreased from 7.45±5.1% to 4.78±4.1% for the consolidated and distributed meta-structures respectively. In combination, the results suggest that the structural arrangement of the pre-mix ingredients significantly effects the post-mix material composition and void content (**Figure 16 and Figure 17**).

## 3.3. MECHANICAL CHARACTERIZATION

To explore the potential influence of pre-mix meta-structure on the mechanical performance of post-mix products (a metric of mix homogeneity), we conducted tensile tests using cured post-mix dog bones.

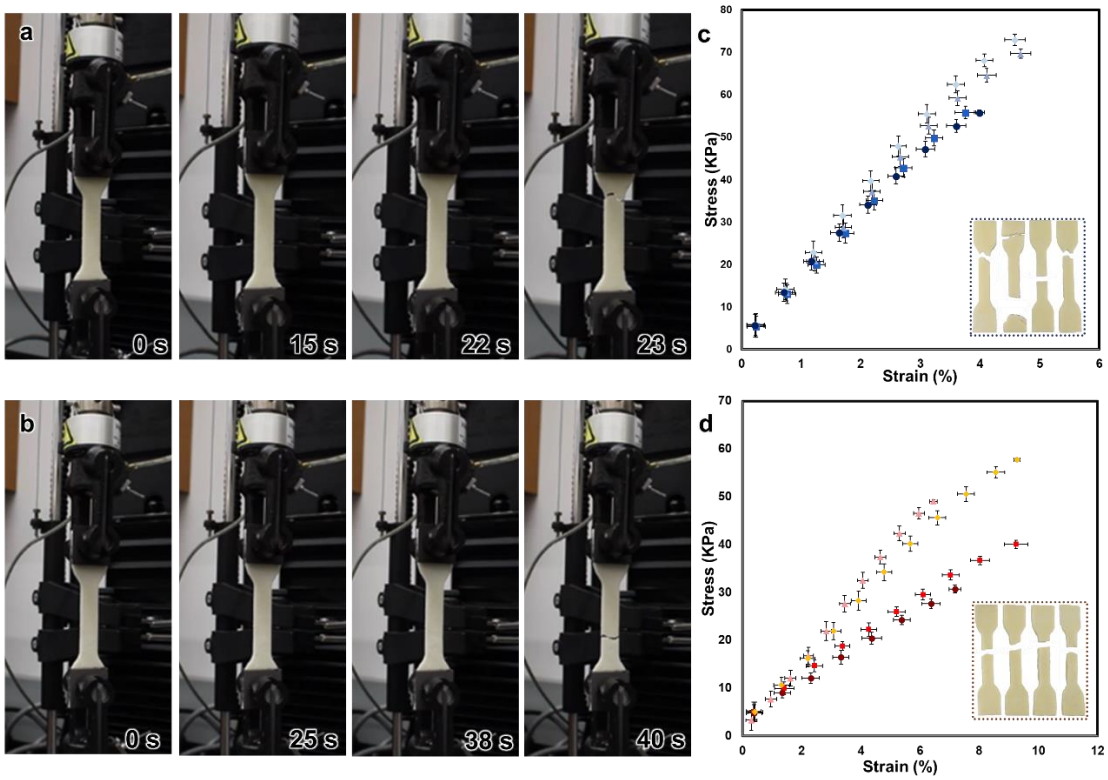


**Figure 18:** Mechanical characterization results. **(a, b)** Sequential images of uniaxial tensile testing of post-mix dog bones corresponding to consolidated **(a)** and distributed **(b)** pre-mix meta-structures. **(c, d)** Quantified results for percent elongation before fracture corresponding to consolidated **(c)** and distributed **(d)** pre-mix meta-structures for four specimens. Inset images = dog bones after failure.

Using and Instron 3345, we individually subjected four dog bone specimens corresponding to each pre-mix meta-structure design ($n$ = 8 total specimens) to a strain rate of 5 mm/min at 20˚C until failure (**Figure 18a-b**). Quantified experimental results revealed significantly larger percent elongation for the distributed meta-structure cases compared to the consolidated specimens (**Figure 18c-d**). For example, the largest observed percent elongation prior to failure for the consolidated case was 4.68%±0.17%, a dramatic reduction from the largest elongation for the distributed meta-structure case of 9.27%±0.11%. Mechanical testing of post-mix products revealed that the distributed meta-structure specimens elongated up to 147% more than the consolidated specimens prior to fracture. Consistent with the optical

characterization results, the disparities in mechanical behavior associated with the two pre-mix meta-structure designs also suggests a significant role for pre-mix ingredient structure in post-mix performance.

# 4. CONCLUSIONS

The objective of this project was to advance the current scientific understanding of the PSP relationships underlying RAM, particularly with respect to the influence of the relative structural arrangement of pre-mix ingredients on post-mix outcomes. We developed and implemented a novel embedded additive manufacturing strategy for the controlled deposition and placement of distinct pre-mix ingredients. Experiments conducted with energetic surrogates revealed that pre-mix meta-structure serves as a critical determinant of post-mix properties and performance—a result not previously reported anywhere in literature. In particular, the optical characterization of post-mix specimens revealed that microstructural defect formation appeared to be a function of the pre-mix meta-structure, with the specially distributed pre-mix meta-structure leading to dramatic reductions in the void content (**Figure 16**) and AVA (**Figure 17**). Similarly, post-mix specimens for the distributed pre-mix meta-structure case exhibited significantly improved elongation behavior prior to failure during tensile testing (**Figure 18**). The dramatic differences in post-mix outcomes suggest that further study of additional pre-mix meta-structures is warranted. Correspondingly, by extending the additive manufacturing-based approaches in this project, it may be possible to tailor pre-mix meta-structure designs for targeted applications, providing promising new means to support industries that rely on energetics.

# 5. FUTURE WORK

An important next step for this work is to investigate alternative additive manufacturing approaches to the process illustrated in **Figure 4**. Specifically, one of the potential issues associated with the embedded printing concept is that the act of plunging the needle into the solids, which is required for each deposition step, may introduce undesired shock to the solids. Although this issue is not a concern for this project in which tests of pre-mix meta-structure *versus* post-mix performance were conducted using inert materials, it would be non-ideal for future uses of this work for RAM processing of non-surrogate energetics. As such, we propose a full 3D printing approach, which would involve additively manufacturing, not only the HTPB-IDP-lecithin wetting agent and IDPI curing agents, but also the solid surrogate particles.

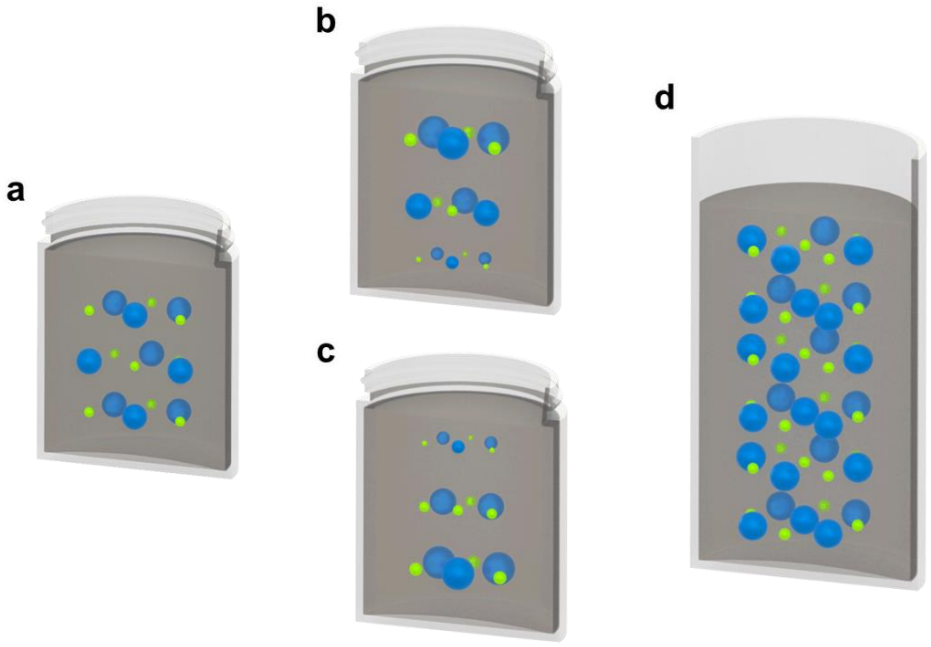


**Figure 19:** Conceptual illustration of possible future distributed meta-structures. The goal being to achieve the same uniformity, that was noted in the middle sections, throughout the meta-structure. **(a)** distributed meta-structure tested in this experiment, **(b)** possible future distributed meta-structure with larger bulk liquid aliquots

comprising of HTPB-IDP-lecithin wetting agent, as well as larger curing agent aliquots of IPDI in top section compared to lower section, **(c)** possible future distributed meta-structure with larger bulk liquid aliquots comprising of HTPB-IDP-lecithin wetting agent, as well as larger curing agent aliquots of IPDI in bottom section compared to top section, **(d)** possible future distributed meta-structure showing a L/D ration greater than one while maintaining consistent bulk liquid aliquots comprising of HTPB-IDP-lecithin wetting agent, as well as consistent curing agent aliquots of IPDI in all layers.

The results of this project revealed significant benefits to implementing the distributed pre-mix meta-structure for influence post-mix outcomes; however, only a single distributed meta-structure was investigated. In **Figure 16**, for instance, the results revealed significant disparities in defect content along the height of the post-mix product for the distributed meta-structure case. Such anomalies suggest that further study of additional pre-mix meta-structure designs is warranted. Of the many options to design a pre-mix meta-structure, **Figure 19b and c** show two options. Both options adjust the local volume of the bulk and curative that is distributed throughout the pre-mix meta-structure while maintaining the total volume in the meta-structure constant. These pre-mix meta-structures are aimed at reducing the RVC (**Figure 16**) and the AVA (**Figure 17**) which were both noted to be larger in the top sections of the meta-structure.

Lastly, the mix vessel used in this study was cylindrical with an L/D ratio close to 1. Given the mixing challenges associated with large L/D vessels, there is the possibility that extensions of the presented pre-mix meta-structure (**Figure 19d**) additive manufacturing could enhance mixing in such containers as well as more complex geometries to support mix-in-case capabilities. As there is no prior work in either of these areas, there is considerable potential that research centering on such

activities could provide new overmatch capabilities stemming from advances in energetics manufacturing and production.

# APPENDIX A: EXAMPLE OF G-CODE

```
M118 10:1 | 1.5X | OLD
;BULK: 269.68 | 134.34
;CURE: 13.93


M118 Homing
G90
M42 P57 S0
G4 S2
M280 P0 S0
G4 S2
M42 P57 S255
G28 X0 Y0
G28 Z0
G1 Z50 F4000
G1 X131 Y96.6 F4000
G4 S2


M117 Bulk First Layer
T0
M42 P57 S0
G4 S2
M280 P0 S97
G4 S2
M42 P57 S255
G91

M0 Start Bulk Layer 1?

M117 M | M | First Layer
M42 P57 S255
G4 S2
G1 Z-43 F100
G1 E134.34 F1000
G4 S15
G1 E134.34 F1000
G4 S15
G1 Z43 F4000

M117 B | L | First Layer
M42 P57 S255
G4 S2
G1 X-12.056 Y-12.056
```

```
G1 Z-43 F100
G1 E134.34 F1000
G4 S15
G1 E134.34 F1000
G4 S15
G1 Z43 F4000

M117 B | R | First Layer
M42 P57 S255
G4 S2
G1 X24.112
G1 Z-43 F100
G1 E134.34 F1000
G4 S15
G1 E134.34 F1000
G4 S15
G1 Z43 F4000

M117 T | R | First Layer
M42 P57 S255
G4 S2
G1 Y24.112
G1 Z-43 F100
G1 E134.34 F1000
G4 S15
G1 E134.34 F1000
G4 S15
G1 Z43 F4000

M117 T | L | First Layer
M42 P57 S255
G4 S2
G1 X-24.112
G1 Z-43 F100
G1 E134.34 F1000
G4 S15
G1 E134.34 F1000
G4 S15
G1 Z43 F4000
G90
G1 Z50
G1 X131 Y96.6 F4000


M117 Curative First Layer
M42 P57 S255
```

```
G4 S2
T1
M42 P57 S0
G4 S2
M280 P0 S175
G4 S2
M42 P57 S255
G91
M0 Start Cure Layer 1?

M117 B | M | First Layer
M42 P57 S255
G4 S2
G1 Y-17.05
G1 Z-43 F100
G1 E13.93 E1000
G4 S30
G1 Z43 F4000
G1 Y17.05

M117 M | R | First Layer
M42 P57 S255
G4 S2
G1 X17.05
G1 Z-43 F100
G1 E13.93 E1000
G4 S30
G1 Z43 F4000
G1 X-17.05

M117 T | M | First Layer
M42 P57 S255
G4 S2
G1 Y17.05
G1 Z-43 F100
G1 E13.93 E1000
G4 S30
G1 Z43 F4000
G1 Y-17.05

M117 M | L | First Layer
M42 P57 S255
G4 S2
G1 X-17.05
G1 Z-43 F100
G1 E13.93 E1000
```

```
G4 S30
G1 Z43 F4000
G1 X17.05
G90
G1 Z50
G1 X131 Y96.6 F4000


M117 Curative Second Layer
T1
G4 S2
M42 P57 S0
G4 S2
M280 P0 S175
G4 S2
M42 P57 S255
G91

M0 Start Cure Layer 2?

M117 M | M | Second Layer
M42 P57 S255
G4 S2
G1 Z-34 F100
G1 E13.93 E1000
G4 S30
G1 Z34 F4000

M117 B | L | Second Layer
M42 P57 S255
G4 S2
G1 X-12.056 Y-12.056
G1 Z-34 F100
G1 E13.93 E1000
G4 S30
G1 Z34 F4000

M117 B | R | Second Layer
M42 P57 S255
G4 S2
G1 X24.112
G1 Z-34 F100
G1 E13.93 E1000
G4 S30
G1 Z34 F4000
```

M117 T | R | Second Layer
M42 P57 S255
G4 S2
G1 Y24.112
G1 Z-34 F100
G1 E13.93 E1000
G4 S30
G1 Z34 F4000

M117 T | L | Second Layer
M42 P57 S255
G4 S2
G1 X-24.112
G1 Z-34 F100
G1 E13.93 E1000
G4 S30
G1 Z34 F4000
G90
G1 Z50
G1 X131 Y96.6 F4000

M117 Bulk Second Layer
M42 P57 S255
G4 S2
T0
M42 P57 S0
G4 S2
M280 P0 S97
G4 S2
M42 P57 S255
G91

M0 Start Bulk Layer 2?

M117 B | M | Second Layer
M42 P57 S255
G4 S2
G1 Y-17.05
G1 Z-34 F100
G1 E134.34 F1000
G4 S15
G1 E134.34 F1000
G4 S15

```
G1 Z34 F4000
G1 Y17.05

M117 M | R | Second Layer
M42 P57 S255
G4 S2
G1 X17.05
G1 Z-34 F100
G1 E134.34 F1000
G4 S15
G1 E134.34 F1000
G4 S15
G1 Z34 F4000
G1 X-17.05

M117 T | M | Second Layer
M42 P57 S255
G4 S2
G1 Y17.05
G1 Z-34 F100
G1 E134.34 F1000
G4 S15
G1 E134.34 F1000
G4 S15
G1 Z34 F4000
G1 Y-17.05

M117 M | L |Second Layer
M42 P57 S255
G4 S2
G1 X-17.05
G1 Z-34 F100
G1 E134.34 F1000
G4 S15
G1 E134.34 F1000
G4 S15
G1 Z34 F4000
G1 X17.05
G90

M117 Home
G1 Z50
G1 X131 Y96.6 F4000
```

M0 Start Bulk Layer 3?

M117 Bulk Third Layer
T0
G4 S2
G91

M117 M | M | Third Layer
M42 P57 S255
G4 S5
G1 Z-25 F100
G1 E134.34 F1000
G4 S15
G1 E134.34 F1000
G4 S15
G1 Z25 F4000

M117 B | L | Third Layer
M42 P57 S255
G4 S5
G1 X-12.056 Y-12.056
G1 Z-25 F100
G1 E134.34 F1000
G4 S15
G1 E134.34 F1000
G4 S15
G1 Z25 F4000

M117 B | R | Third Layer
M42 P57 S255
G4 S5
G1 X24.112
G1 Z-25 F100
G1 E134.34 F1000
G4 S15
G1 E134.34 F1000
G4 S15
G1 Z25 F4000

M117 T | R | Third Layer
M42 P57 S255
G4 S5
G1 Y24.112
G1 Z-25 F100
G1 E134.34 F1000
G4 S15

G1 E134.34 F1000
G4 S15
G1 Z25 F4000

M117 T | L | Third Layer
M42 P57 S255
G4 S5
G1 X-24.112
G1 Z-25 F100
G1 E134.34 F1000
G4 S15
G1 E134.34 F1000
G4 S15
G1 Z25 F4000
G90
G1 Z50
G1 X131 Y96.6 F4000

M0 Start Cure Layer 3?

M117 Curative Third Layer
M42 P57 255
G4 S5
T1
M42 P57 S0
G4 S5
M280 P0 S175
G4 S5
M42 P57 S255
G91

M117 B | M | Third Layer
M42 P57 S255
G4 S5
G1 Y-17.05
G1 Z-25 F100
G1 E13.93 E1000
G4 S30
G1 Z25 F4000
G1 Y17.05

M117 M | R | Third Layer
M42 P57 S255
G4 S5
G1 X17.05

```
G1 Z-25 F100
G1 E13.93 E1000
G4 S30
G1 Z25 F4000
G1 X-17.05

M117 T | M | Third Layer
M42 P57 S255
G4 S5
G1 Y17.05
G1 Z-25 F100
G1 E13.93 E1000
G4 S30
G1 Z25 F4000
G1 Y-17.05

M117 M | L | Third Layer
M42 P57 S255
G4 S5
G1 X-17.05
G1 Z-25 F100
G1 E13.93 E1000
G4 S30
G1 Z25 F4000
G1 X17.05

G90
G1 Z50
G1 X131 Y96.6 F4000
G1 X0 Y0
M118 FINISHED!!
G4 S5
```

# APPENDIX B: SEM AND EDS IMAGES

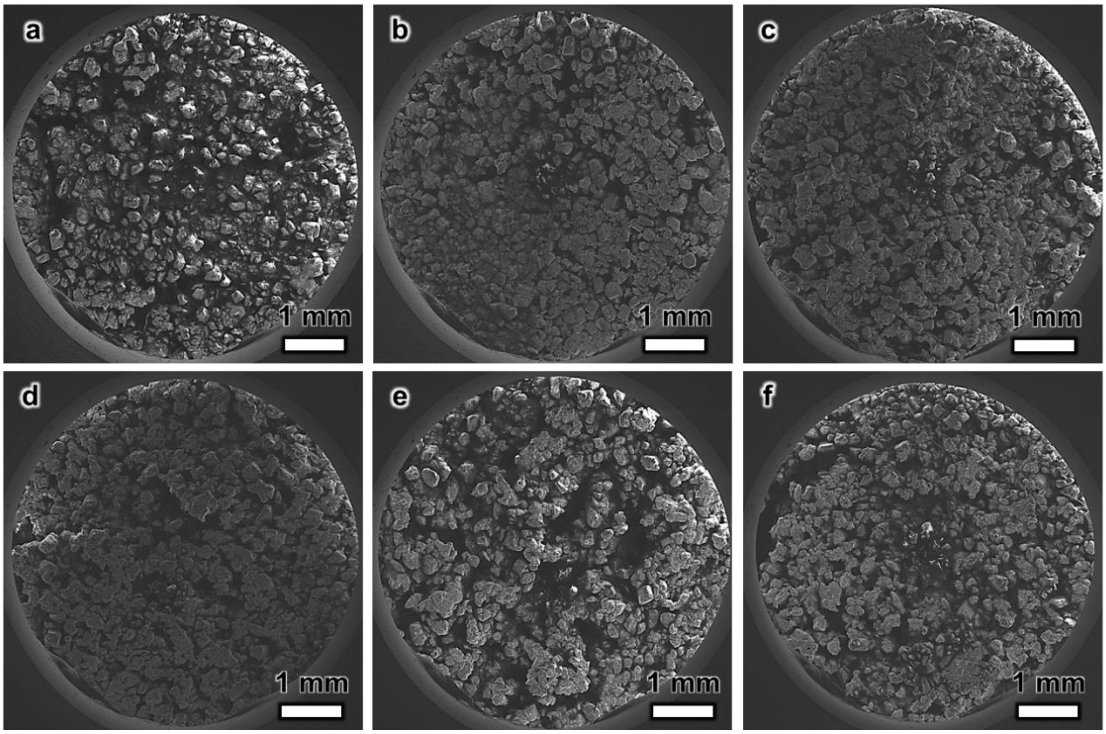


**Figure 20:** Distributed pre-mix meta-structure SEM images of sections following RAM processing; **(a, b)** top, **(c, d)** middle, and **(e, f)** bottom.

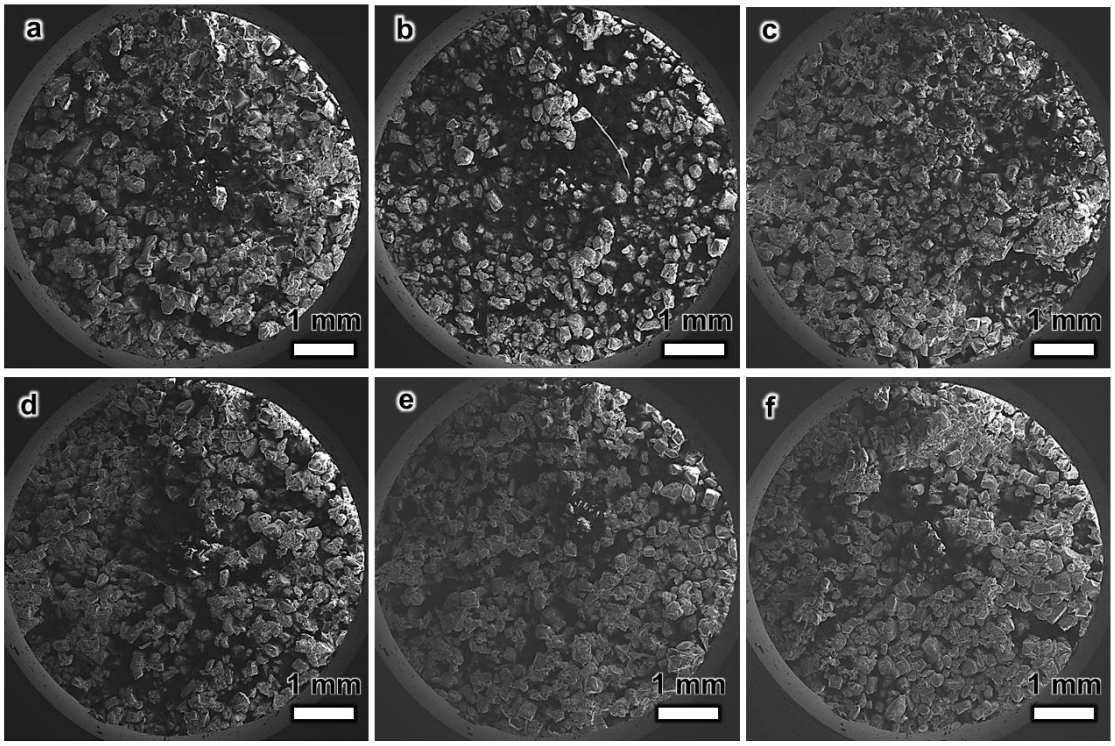


**Figure 21:** Consolidated pre-mix meta-structure SEM images of sections following RAM processing; **(a, b)** top, **(c, d)** middle, and **(e, f)** bottom.

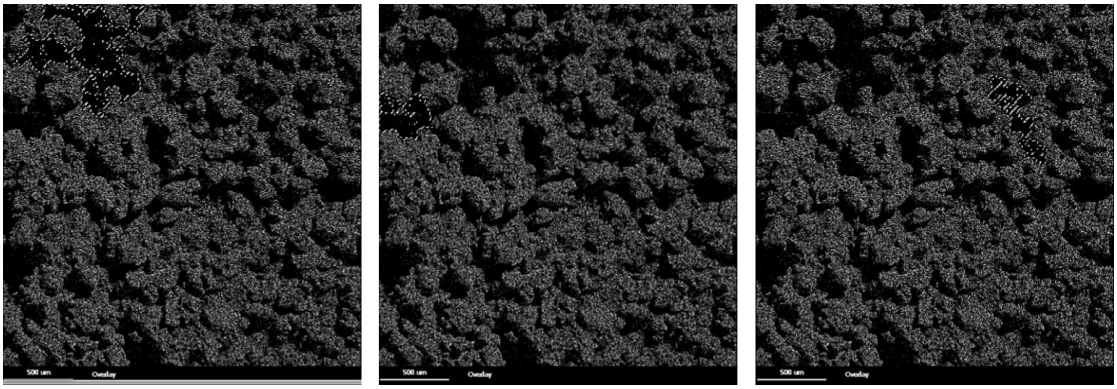

**Figure 22:** EDS images showing the largest three areas selected in the first sample for the top section of the distributed meta-structure.

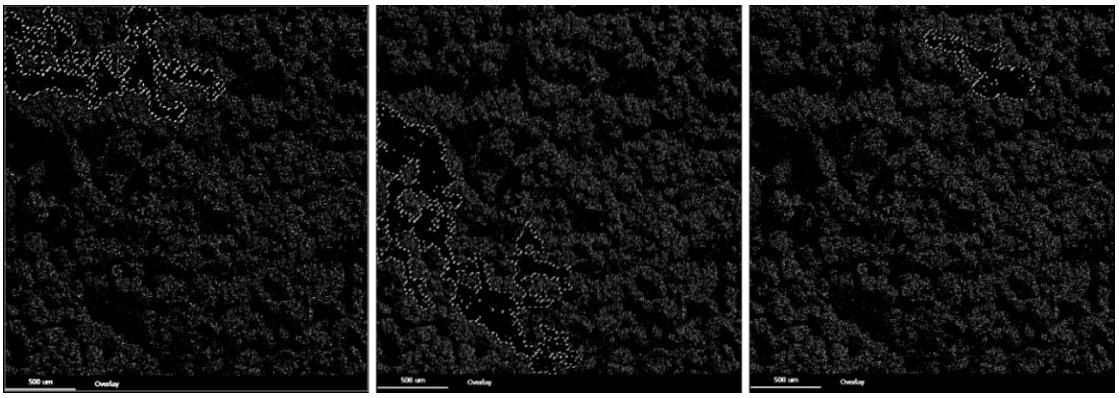

**Figure 23:** EDS images showing the largest three areas selected in the second sample for the top section of the distributed meta-structure.

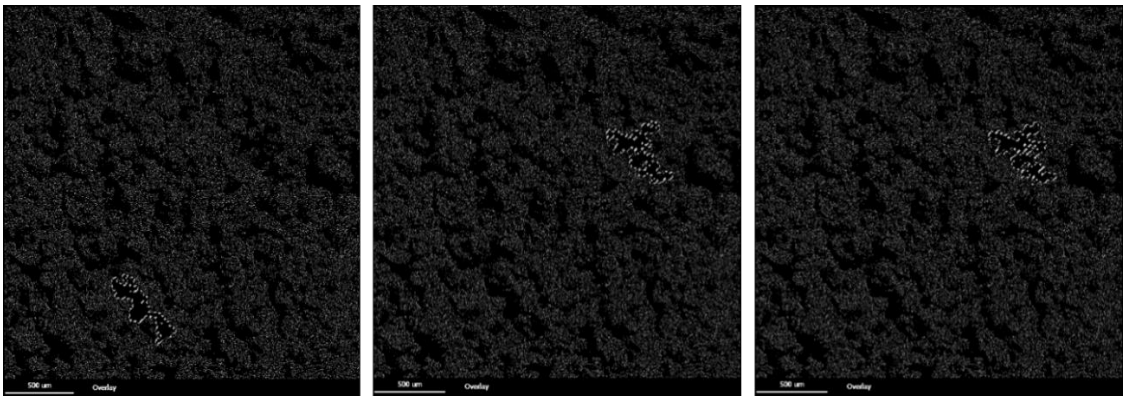

**Figure 24:** EDS images showing the largest three areas selected in the first sample for the middle section of the distributed meta-structure.

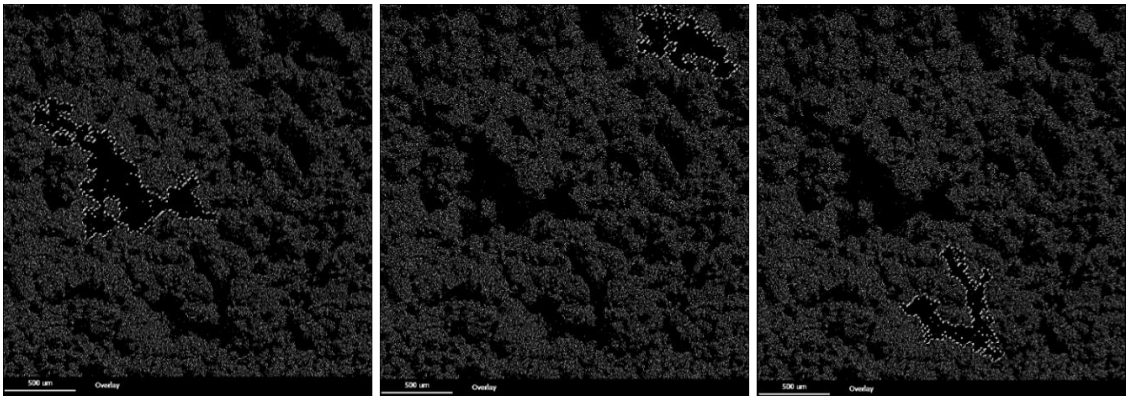

**Figure 25:** EDS images showing the largest three areas selected in the second sample for the middle section of the distributed meta-structure.

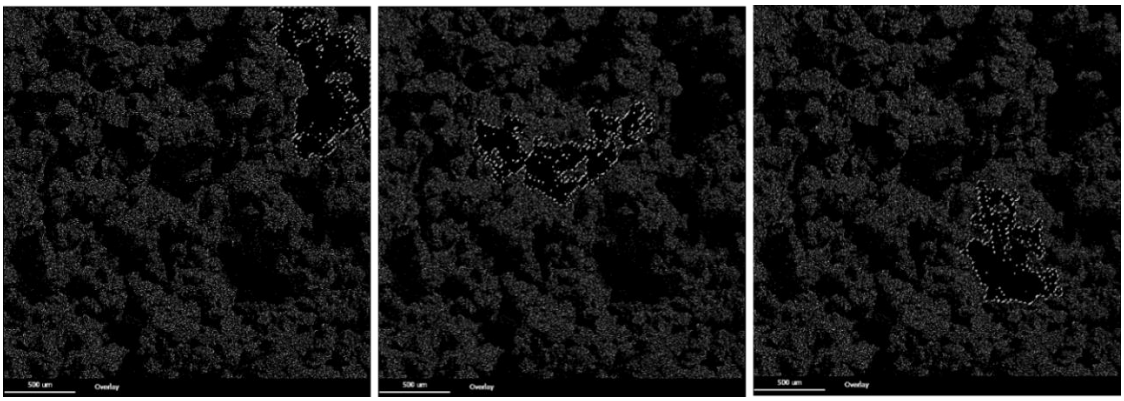

**Figure 26:** EDS images showing the largest three areas selected in the first sample for the bottom section of the distributed meta-structure.

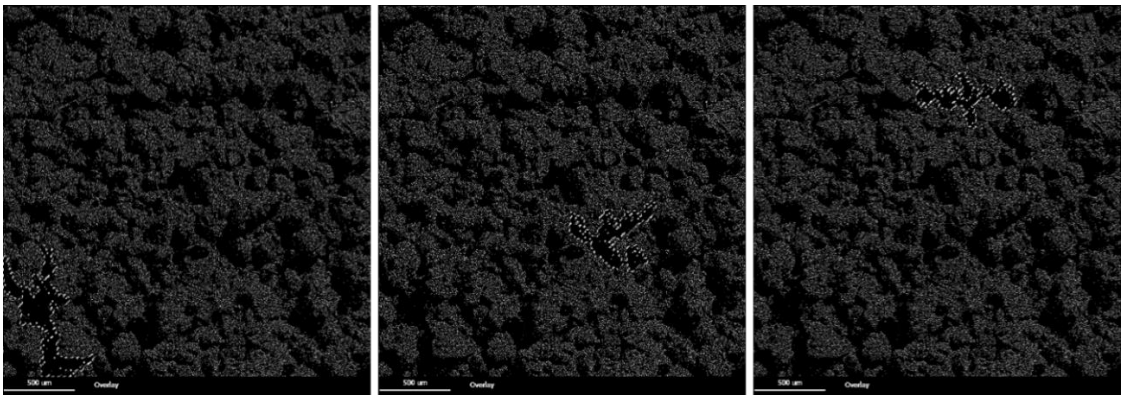

**Figure 27:** EDS images showing the largest three areas selected in the second sample for the bottom section of the distributed meta-structure.

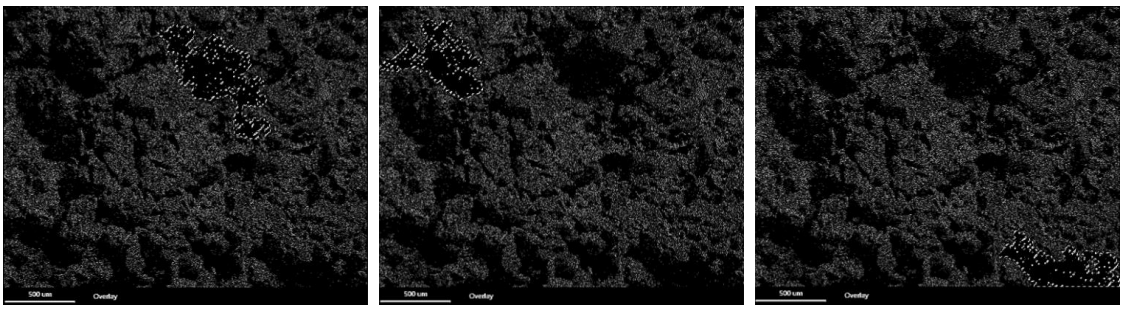

**Figure 28:** EDS images showing the largest three areas selected in the first sample for the top section of the consolidated meta-structure.

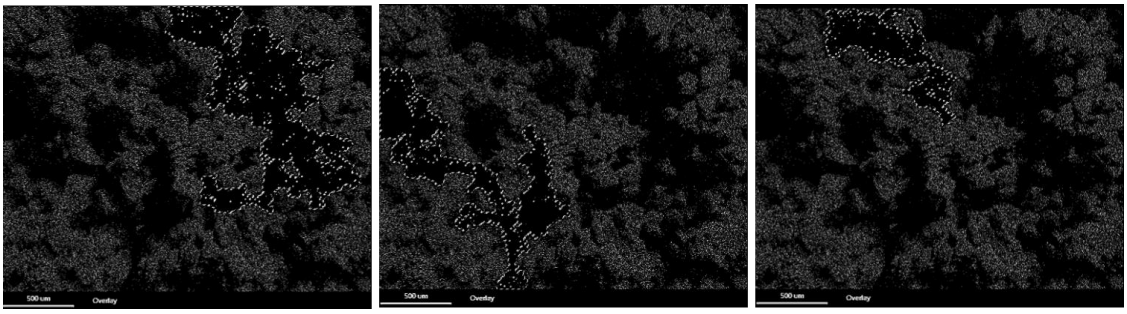

**Figure 29:** EDS images showing the largest three areas selected in the second sample for the top section of the consolidated meta-structure.

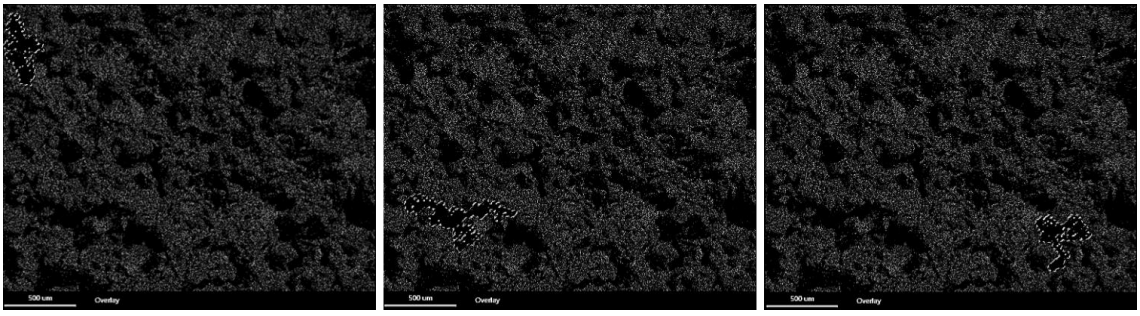

**Figure 30:** EDS images showing the largest three areas selected in the first sample for the middle section of the consolidated meta-structure.

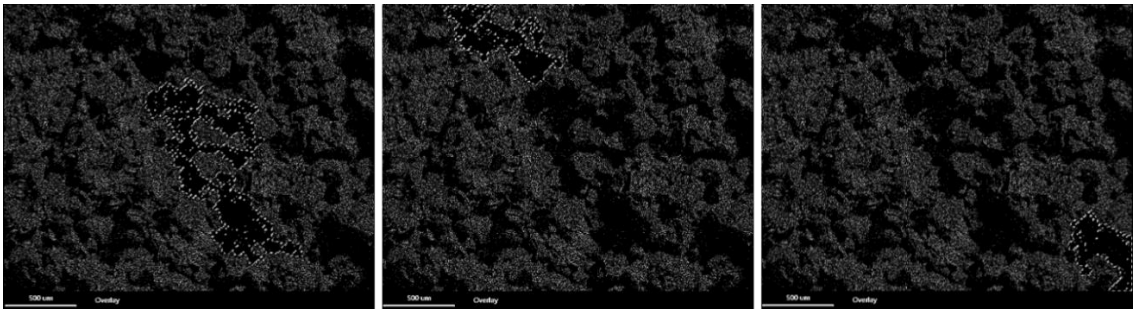

**Figure 31:** EDS images showing the largest three areas selected in the second sample for the middle section of the consolidated meta-structure.

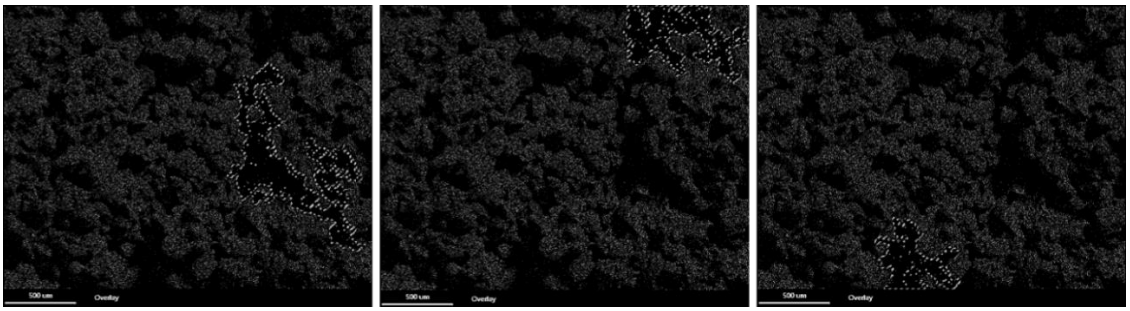

**Figure 32:** EDS images showing the largest three areas selected in the first sample for the bottom section of the consolidated meta-structure.

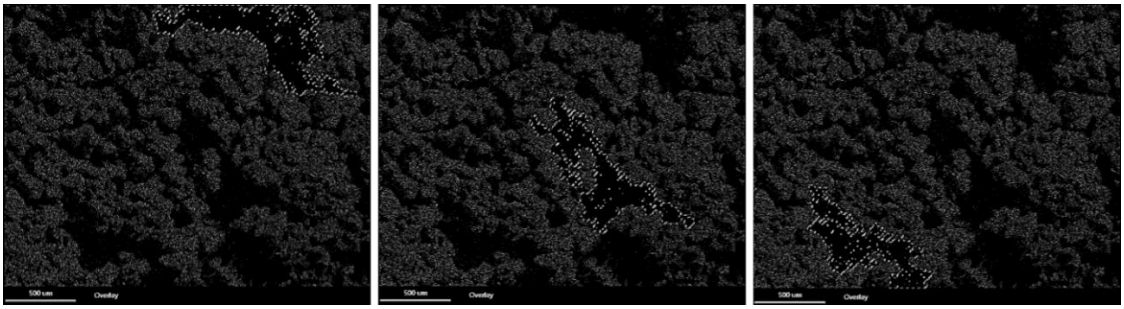

**Figure 33:** EDS images showing the largest three areas selected in the second sample for the bottom section of the consolidated meta-structure.

# APPENDIX C: DATA FROM EDS AREA ANALYSIS

**Table 1:** Computed average data correlating to average void area for the three largest voids measured after EDS imaging.

| | Average Void Area (%) | | SD | |
|---|---|---|---|---|
| | Consolidated | Distributed | Consolidated | Distributed |
| Bottom | 5.40% | 3.82% | 1.61% | 1.90% |
| Middle | 3.33% | 2.43% | 2.63% | 1.70% |
| Top | 7.45% | 4.78% | 4.65% | 3.74% |

# REFERENCES

[1] Kyle T. Sullivan, Joshua D. Kuntz, and Alexander E. Gash. “The role of fuel particle size on flame propagation velocity in thermites with a nanoscale oxidizer. Propellants, Explosives, Pyrotechnics, 39(3):407–415, 2014.

[2] Ryoma Tanaka, Naoyuki Takahashi, Yasuaki Nakamura, Yusuke Hattori, Kazuhide Ashizawa, and Makoto Otsuka. “Verification of the mixing processes of the active pharmaceutical ingredient, excipient and lubricant in a pharmaceutical formulation using a resonant acoustic mixing technology.” *RSC Advances*, 6:87049–87057, 2016.

[3] Yifan Wang, Juan G. Osorio, Tianyi Li, and Fernando J. Muzzio. “Controlled shear system and resonant acoustic mixing: Effects on lubrication and flow properties of pharmaceutical blends.” *Powder Technology*, 322:332–339, 2017.

[4] Juan G. Osorio, Koushik Sowrirajan, and Fernando J. Muzzio. “Effect of resonant acoustic mixing on pharmaceutical powder blends and tablets.” *Advanced Powder Technology*, 27(4):1141–1148, 2016.

[5] Juan G. Osorio, Eduardo Hernndez, Rodolfo J. Romaach, and Fernando J. Muzzio. “Characterization of resonant acoustic mixing using near-infrared chemical imaging.” *Powder Technology*, 297:349–356, 2016.

[6] Dennis H. Leung, David J. Lamberto, Lina Liu, Elizabeth Kwong, Todd Nelson, Timothy Rhodes, and Annette Bak. “A new and improved method for the preparation of drug nanosuspension formulations using acoustic mixing technology.” *International Journal of Pharmaceutics*, 473(1):10–19, 2014.

[7] Karthik Nagapudi *et al.* “High-throughput screening and scale-up of co-crystals using resonant acoustic mixing.” *International Journal of Pharmaceutics*, 521(1):337–345, 2017.

[8] Lu Zhang, Yidong Li, Manal Abed, and Rajesh N. Dav. “Incorporation of surface-modified dry micronized poorly water-soluble drug powders into polymer strip films.” *International Journal of Pharmaceutics*, 535(1):462–472, 2018.

[9] Stephen R. Anderson *et al*. “Preparation of an energetic-energetic co-crystal using resonant acoustic mixing.” *Propellants, Explosives, Pyrotechnics*, 39(5):637–640, 2014.

[10] David J. am Ende, Stephen R. Anderson, and Jerry S. Salan. “Development and scale-up of co-crystals using resonant acoustic mixing.” *Organic Process Research and Development*, 18(2):331–341, 2014.

[11] Sonia M. Razavi, Gerardo Callegari, German Drazer, and Alberto M. Cuitio. “Toward predicting tensile strength of pharmaceutical tablets by ultrasound

measurement in continuous manufacturing." *International Journal of Pharmaceutics*, 507(1):83 – 89, 2016.

[12] Ryoma Tanaka, Naoyuki Takahashi, Yasuaki Nakamura, Yusuke Hattori, Kazuhide Ashizawa, and Makoto Otsuka. "In-line and real-time monitoring of resonant acoustic mixing by near-infrared spectroscopy combined with chemometric technology for process analytical technology applications in pharmaceutical powder blending systems." *Analytical Sciences*, 33(1):41–46, 2017.

[13] Adam A. L. Michalchuk, Karl S. Hope, Stuart R. Kennedy, Maria V. Blanco, Elena V. Boldyreva, and Colin R. Pulham. "Ball-free mechanochemistry: in situ real-time monitoring of pharmaceutical co-crystal formation by resonant acoustic mixing." *Chemical Communications*, 54:4033–4036, 2018.

[14] Charles D. Papageorgiou, Marianne Langston, Frederick Hicks, David am Ende, Eric Martin, Sarah Rothstein, Jerry Salan, and Robert Muir. "Development of screening methodology for the assessment of the agglomeration potential of apis." *Organic Process Research and Development*, 20(8):1500–1508, 2016.

[15] Ryan L. Truby, Michael Wehner, Abigail K. Grosskopf, Daniel M. Vogt, Sebastien G. M. Uzel, Robert J. Wood, and Jennifer A. Lewis. "Soft Somatosensitive Actuators via Embedded 3D Printing." *Advanced Materials, 30(15). 1706383,* 2018.

[16] Wehner, M., Truby, R., Fitzgerald, D., Mosadegh, B., Whitesides, G., Lewis, J., & Wood, R. "An integrated design and fabrication strategy for entirely soft, autonomous robots." *Nature, 536(7617), 451-455*. 2016.

[17] Hinton, T., Hudson, A., Pusch, K., Lee, A., & Feinberg, A. "3D Printing PDMS elastomer in a hydrophilic support bath via freeform reversible embedding." *Acs Biomaterials Science & Engineering, 2(10), 1781-1786*. 2016.

[18] Muth, J., Vogt, D., Truby, R., Mengüç, Y., Kolesky, D., Wood, R., & Lewis, J. "Embedded 3D printing of strain sensors within highly stretchable elastomers." *Advanced Materials, 26(36), 6307-6312.* 2014.

[19] Grosskopf, A., Truby, R., Kim, H., Perazzo, A., Lewis, J., & Stone, H. "Viscoplastic matrix materials for embedded 3D printing." *Acs Applied Materials & Interfaces, 10(27), 23353-23361*. 2018.

[20] James T Miller, David A Bode, and Scott Coguill. "Resonant acoustic mixing; design and process considerations concerning vessel/case geometry and mix versus cure time when preparing composite solid propellant." *JANNAF 36th Propellant and Explosives Development and Characterization Joint Subcommittee Meeting*, 2010.

[21] M. Jawaid, H.P.S. Abdul Khalil, A. Abu Bakar, P. Noorunnisa Khanam. "Chemical resistance, void content and tensile properties of oil palm/jute fiber reinforced polymer hybrid composites." *Materials & Design, 32(2):1014-1019,* 2011.

[22] Francois LeBei, Edu Ruiz, Francois Trochu. "Void content analysis and processing issues to minimize defects in liquid composite molding." *Polymer Composites, 40(1):109-120,* 2019.

[23] Haolong Liu, Haitao Cui, Weidong Wen, Xuming Su, Hongtae Kang, and Carlos Engler-Pinto. "The effect of voids on the quasi-static tensile properties of carbon fiber/polymer laminated composites." *Journal of Composite Materials, 52(15): 1997-2015,* 2018.